# Single-Molecule Tracking of Chromatin-Associated Proteins in the *C. elegans* Gonad

Lexy von Diezmann* and Ofer Rog*

Cite This: https://doi.org/10.1021/acs.jpcb.1c03040

Read Online

ACCESS | 📊 Metrics & More | 📄 Article Recommendations | 🔲 Supporting Information

**ABSTRACT:** Biomolecules are distributed within cells by molecular-scale diffusion and binding events that are invisible in standard fluorescence microscopy. These molecular search kinetics are key to understanding nuclear signaling and chromosome organization and can be directly observed by single-molecule tracking microscopy. Here, we report a method to track individual proteins within intact *C. elegans* gonads and apply it to study the molecular dynamics of the axis, a proteinaceous backbone that organizes meiotic chromosomes. Using either fluorescent proteins or enzymatically ligated dyes, we obtain multisecond trajectories with a localization precision of 15–25 nm in nuclei actively undergoing meiosis. Correlation with a reference channel allows for accurate measurement of protein dynamics, compensating for movements of the nuclei and chromosomes within the gonad. We find that axis proteins exhibit either static binding to chromatin or free diffusion in the nucleoplasm, and we separately quantify the motion parameters of these distinct populations. Freely diffusing axis proteins selectively explore chromatin-rich regions, suggesting they are circumventing the central phase-separated region of the nucleus. This work demonstrates that single-molecule microscopy can infer nanoscale-resolution dynamics within living tissue, expanding the possible applications of this approach.
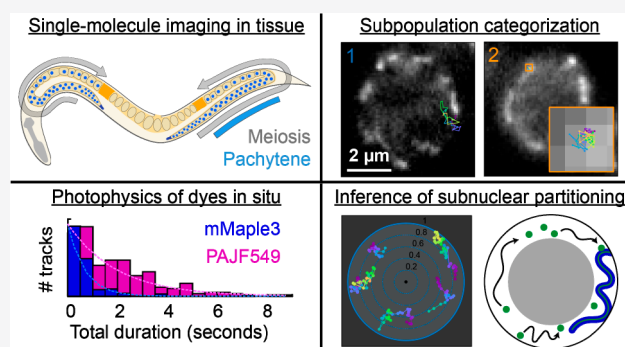
## 1. INTRODUCTION

The nucleus is the storage compartment for a cell's genome but is also dynamically organized to enable many complex processes. These include the duplication, condensation, and partitioning of chromosomes during cell division, the regulation of transcription by chromatin packaging and recruited proteins, and ribosome biogenesis, which occurs in the nucleolus. Meiosis—the specialized cell-division cycle that produces gametes such as sperm, egg, and pollen and underlies sexual reproduction—is one such specialized process. During meiotic prophase, parental chromosome pairs are juxtaposed and undergo DNA breakage and repair to generate physical linkages (crossovers) between chromosomes that are used to correctly partition chromosomes into gametes.[1,2] Fundamental to meiosis is the unique packaging adopted by meiotic chromosomes, as a series of loops anchored at their base to a protein complex known as the meiotic axis (Figure 1). This structure is universally conserved and is essential to almost all aspects of the meiotic program, including the alignment of the parental chromosomes and crossover repair. Extensive analyses have defined the localization of and binding interfaces between the protein components of the axis.[3-5]

In multicellular organisms, meiosis occurs in specialized organs and tissues and often in restricted developmental windows. While some of the molecular components and their biochemical activities have been functionally reconstituted *in vitro*, many aspects of their regulation in the context of intact chromosomes remain poorly understood. The nematode *Caenorhabditis elegans* is a particularly convenient system for microscopic studies of meiosis, as it is genetically tractable and the developing gametes within its gonad are ordered in a temporal gradient, allowing different meiotic stages to be easily visualized (Figure 1A).[6] Moreover, chromosomes in meiotic nuclei are arranged so that they are separate from one another, allowing tracing of individual chromosomes in intact samples. Chemical fixation of extruded gonads for high-resolution microscopy has become a commonplace protocol,[7] and super-resolution imaging of such samples has measured the fine structure of the axis and its distinct morphology at different stages of crossover formation.[4,8]
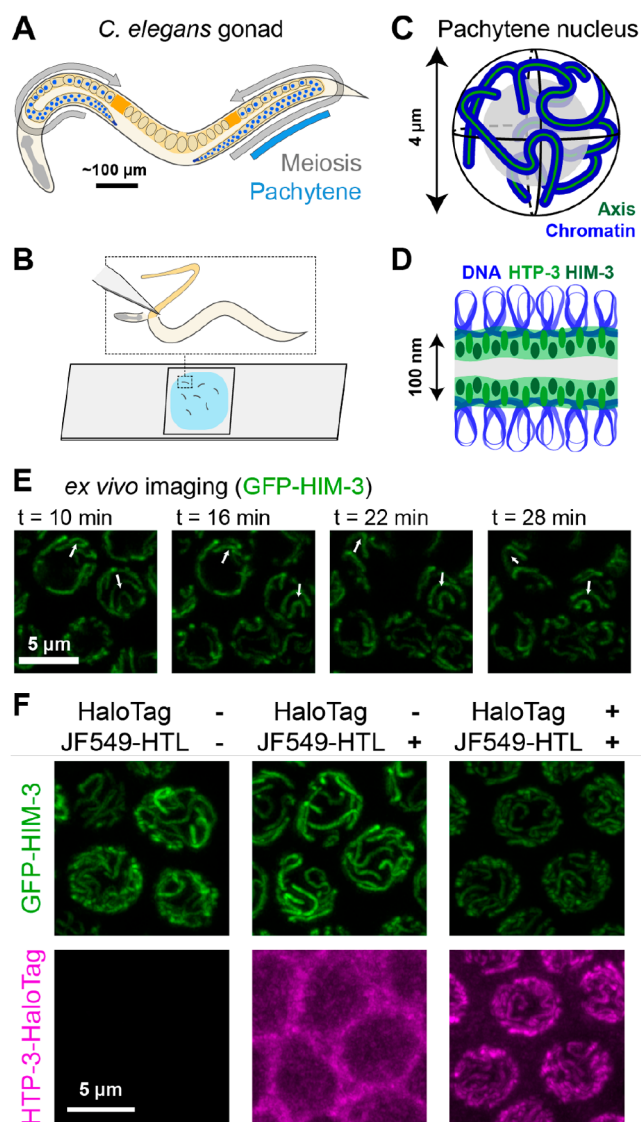
**Figure 1.** Imaging in the *ex vivo* gonad. (A) Schematic of *C. elegans* with both gonad arms marked. Meiosis progresses linearly along the gonad (gray arrows), with the pachytene stage occurring in approximately the middle third (blue line). (B) Schematic of gonad extrusion. Top: manual dissection of *C. elegans* extrudes the gonad into solution while remaining supported by attachment to the main body of the worm. Bottom: many extruded gonads are immobilized between an agarose pad and a coverslip mounted on a microscope slide. (C) Approximate geometry of the six chromosomes of *C. elegans* during pachytene. Blue, chromatin; green, axis; gray, nucleolus. (D) The nanoscale geometry of looped chromosomal DNA (blue) and the meiotic axis (green). In worms, two major axis protein components are HTP-3 and HIM-3. (E) Meiotic nuclei maintain function for tens of minutes following dissection. Images are partial maximum intensity projections of nuclei expressing GFP-labeled HIM-3, which marks the meiotic axis. Arrows highlight the chromosome motion that characterizes this stage of meiosis. (F) The gonad is permeable for the synthetic dye JF549 functionalized with a HaloTag ligand (HTL), allowing labeling of HTP-3 fused to the HaloTag enzyme. Partial maximum intensity projections of nuclei are shown for clarity. The image contrast for the GFP and JF549 channels is kept the same between conditions where the HTP-3-HaloTag fusion is present ("HaloTag") and the dye is or is not added ("JF549-HTL"). Note the colocalization of GFP-HIM-3 and HTP-3-HaloTag, indicating broadly unperturbed localization of HTP-3-HaloTag.

In recent years, many advancements have been made by a suite of techniques that probe the dynamics of chromatin-associated proteins.[9−14] A key component of these efforts has been the application of single-molecule techniques *in vitro* and *in vivo*. Rather than bulk measurements reflecting the average behavior of thousands or more molecules, single-molecule methods have the ability to reveal underlying heterogeneity that is invisible at the population level.[15] By localizing single molecules in cells, it is possible not only to achieve super-resolution imaging of structure but also to track the motion of single molecules to detect spatiotemporal dynamics.[16] While single-particle tracking has predominantly been used in single-celled organisms and cultured cell monolayers, several studies have shown it is possible to extend this method to *ex vivo* tissue slices[17,18] and developing embryos.[19−22] However, these approaches have not been widely applied, possibly due to the need for light-sheet illumination to image within thick tissues.[20]

In this work, we demonstrate an approach to track single molecules within *C. elegans* gonads, allowing the study of protein dynamics in metazoan meiosis using a standard single-molecule microscope. This development overcomes two major challenges. First, to attain high-resolution images while also watching live-cell dynamics, it was necessary to preserve meiotic function in extruded gonad tissue. Second, it was necessary to find labels that were compatible with live-cell imaging and that were sufficiently photostable to provide long tracks, characteristics not guaranteed for many labels used for super-resolution imaging.[16] We selected the axis proteins HIM-3 and HTP-3 as targets to evaluate our single-molecule tracking approach because of their critical role in meiosis, well-characterized localization and dynamics, and low turnover when bound within a protein complex.[4,23] Using a nutrient-rich buffer allowed us to preserve meiotic function, while imaging in extruded gonads allowed us to introduce highly photostable dyes optimized for single-molecule imaging.[24] We tracked axis proteins with 15−25 nm precision for up to several seconds and discriminated bound and diffusive modes of motion. By analyzing the subpopulation of freely diffusing molecules, we found that diffusing axis proteins are excluded from the nucleolus, suggesting this membraneless organelle affects the motion of chromatin-associated proteins throughout the nucleus.

## 2. METHODS

**Worm Strains and Transgenes.** All strains were cultured by using standard methods.[25] Worms were maintained at 20 °C except as noted. Strains used were CA1350 (*him-3(ie34-[mMaple3::him-3]) IV*),[23] ROG118 (*him-3(gfp::him-3 IV)*),[26] ROG128 (*htp-3(slc2[htp-3::halotag] I*), ROG213 (*htp-3(slc2-[htp-3::halotag]) I, him-3(gfp::him-3) IV*), and CA1330 (*htp-3(tm3655) I; ieSi6 [htp-3::gfp] II; itIs37 [pie-1p::mCherry::H2B::pie-1 3′UTR + Cbr-unc-119(+)] IV*).[27,28] ROG128 (*slc2, htp-3::halotag*) was constructed by CRISPR-Cas9 insertion of a *halotag* construct[29] optimized for germline expression (based on pCFJ2059[30]). This construct was targeted to the C-terminus of the genomic *htp-3* locus, following a 13 a.a. linker (STSGGSGGTGGSS), by using the sgRNA GAGGA-AACTGAacgatttc (capitalization indicates the coding region of the *htp-3* gene). Insertion of *halotag* in the middle of the sgRNA sequence prevented recutting upon successful integration of the repair template. ROG213 was generated by crossing ROG118 with ROG128. As a proxy for the functionality of the tagged axis proteins we quantified hermaphrodite self-progeny (Figure S1): total progeny and male counts were performed by singling L4

hermaphrodites, transferring them to a new plate each day for 3 days, and then counting progeny and males from each plate. HTP-3-HaloTag exhibited meiotic defects, manifesting as lower viable progeny and an increased ratio of males. However, the production of some viable progeny indicates it is at least partly functional. In addition, HTP-3-HaloTag colocalized with HIM-3, as expected (Figure 1D).[31]

**Sample Preparation.** JF549-PEG-HTL (JF549-poly-(ethylene glycol) linker-HaloTag ligand) and PAJF549-HTL (photoactivatable JF549-HaloTag ligand) (gift of Luke Lavis lab, care of Erik Jorgensen lab) were stored at −80 °C as 100 and 20 μM aliquots in DMSO. Immediately before use, aliquots were diluted into M9 minimal medium and then into ECM for labeling during dissections at a final concentration of 10 nM.

Dissection was performed in an adapted embryonic culture medium[32] to preserve native meiotic function. We refer to the medium as ECM, and it is composed of 84% Leibowitz L-15 without phenol red, 9.3% fetal bovine serum, 0.01% levamisole, and 2 mM EGTA, filtered through a 0.2 μm filter and stored in aliquots at −20 °C until use. We measured this preparation to have an osmolarity of 330 mOsm (Advanced Instruments Microsmometer 3300), in line with typical osmolarities used when probing the internal environment of *C. elegans* by electrophysiology.[33] Dissection in these conditions consistently yielded at least a subset of gonads that exhibited meiotic chromosome motion over tens of minutes. Notably, the original preparation described in ref 32 includes 4.7% sucrose, which yielded an osmolarity of 500 mOsm and resulted in mild shrinkage of the gonad (data not shown) and was therefore not used.

To test the ability of minimal medium to support gonad function, we also attempted gonad extrusion in a physiological saline buffer without added nutrients (150 mM NaCl, 5 mM KCl, 1 mM MgCl$_2$, 1 mM CaCl$_2$, 10 mM glucose, 15 mM HEPES, pH 7.35, adjusted to 340 mOsm with sucrose). In experiments using this buffer, chromosomes and nuclei did not exhibit persistent motion, indicating meiotic perturbation (data not shown).

For imaging, dissected gonads were placed onto agarose pads. Typically, 2 drops (∼30 μL) of 2% melted agarose solution in water were dropped to glass slides (VWR Vistavision #16004-422) and flattened by placing another slide on top with thin (∼0.2 mm) spacers of lab tape. Agarose pads were stored in a humid chamber at room temperature. To exchange buffer, ECM was added to the pads before use (two exchanges of 30 μL each, over 10−30 min, with excess liquid aspirated between additions and before adding worms).

Worms were dissected following picking of L4 larvae and incubation for 16−24 h at 25 °C. These staged adult worms were transferred to 20 μL of ECM plus 0.01% Tween 20 and, if used, 10 nM dye. Gonads were extruded by incision directly behind the pharynx with Feather #11 scalpel blades. Approximately 10−15 worms were dissected simultaneously and immediately pipetted onto agarose pads, covered with a 22 × 22 mm² No. 1.5 coverslip (VWR #16004-302), and sealed with VaLaP (1:1:1 Vaseline, lanolin, paraffin). Consistent with previous studies,[32] gonads that incurred damage during dissection did not exhibit physiological chromosome motions; these gonads were not included in our data analysis.

**Microscopy.** Confocal imaging was performed with a Zeiss LSM880 microscope with Airyscan in SR mode (∼49 nm pixel size) equipped with a 1.4NA 63× oil immersion objective (Zeiss Plan-Apochromat). Images were acquired with 3−4% 488 nm laser power, 8% 561 nm laser power, and 1−2 μs pixel dwell times. All images were Airyscan processed (ZEN Blue 2.3), yielding an ∼1.7× resolution enhancement over typical confocal resolution. Radial profile analysis of confocal data was performed by using the Radial Profile Extended ImageJ plugin (Philippe Carl, http://questpharma.u-strasbg.fr/html/radial-profile-ext.html).

Single-molecule microscopy was performed on a Bruker Vutara 352 biplane localization microscope.[34] Briefly, this system provides epi-illumination using collimated continuous-wave lasers (405 nm, 100 mW, Coherent Obis; 488 nm, 1 W, Coherent Genesis; 561 nm, 1 W, Coherent Genesis) modulated with an AOTF and sent through a square iris to provide 40 × 40 μm² square tophat illumination. Data are collected on a Hamamatsu ORCA-Fusion BT sCMOS camera with 99 nm effective pixel size in the image plane. Imaging was performed with a 1.3 NA 60× silicone oil immersion objective (Olympus UPLSAPO60XS2). The irradiances at the image plane used were 0.63 μW/μm² (488 nm), 3.0 μW/μm² (561 nm), and ≤0.23 μW/μm² (405 nm). Molecules were simultaneously excited with 561 nm light and activated with 405 nm light, with the 405 nm irradiance slowly increased over the course of the experiment to maintain a mostly uniform density of activated fluorescent molecules. Acquisition of reference images (488 nm excitation of GFP or preactivation mMaple3) was interleaved with single-molecule imaging, with one reference frame collected every 300 imaging frames (i.e., every 30 s). PSF calibration, camera read noise calibration, single-molecule biplane localization, and signal photon estimation were performed in the Vutara SRX software using established methods.[34,35]

**Single-Molecule Data Analysis.** Calibration of 3D microscope PSFs and single-molecule localization were performed with Vutara SRX software (Bruker). While the biplane modality of the Vutara 352 estimates the three-dimensional position of single molecules because of the relatively poor localization precision in the axial dimension, we analyzed single-molecule data using 2D information only. Track concatenation and mean jump displacement calculations were performed by using the tracking software swift v. 0.4.3 (Endesfelder, M.; Schießl, C.; Turkowyd, B.; Lechner, T.; Endesfelder, U. Manuscript in preparation; software available upon request from www.endesfelder-lab.org). This software performs a global fit of single-molecule data, collecting localizations into trajectories in the most likely way for a given set of prior parameters. We used the following software parameters: p_bleach = 0.05, exp_noise_rate = 5%, p_blink = 0.1, p_reappear = 0.1, exp_displacement = 150 nm, p_switch = 0.005, precision = 25 nm, diffraction_limit = 150 nm, max_displacement = 700 nm, max_particle_count = 1, and max_blinking_duration = 4 frames. Owing to our choice of activation power and density of labeling, each nucleus generally did not contain more than 1−2 actively fluorescing molecules at a time, making tracks straightforward to discriminate.

All further analysis was performed in MATLAB (MathWorks, Inc., Natick, MA). Only localizations within nuclei, defined by the diffraction-limited reference channel (Figure 4B), were used for quantitative analysis.

Mean-squared displacement analysis was performed as previously described.[36] Briefly, we used the 2D diffusion of molecules to estimate diffusivity according to
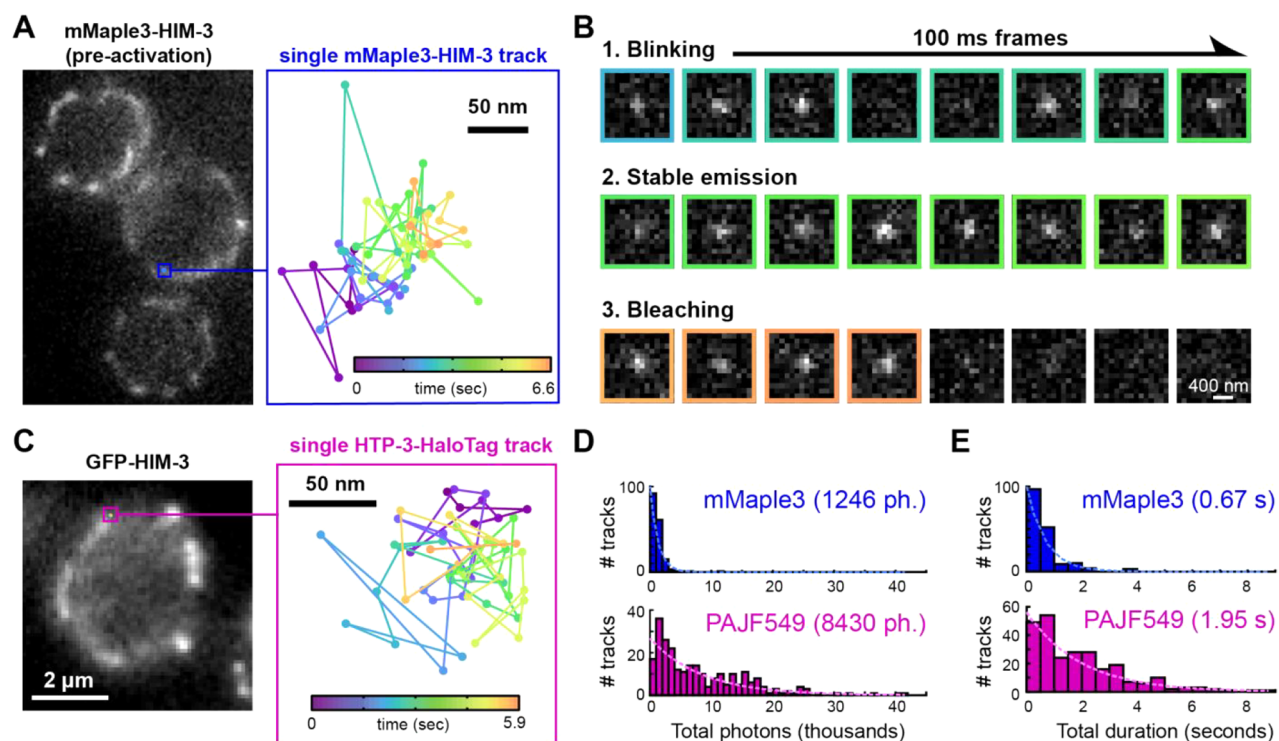
**Figure 2.** Single-molecule imaging of axis proteins. (A) Left: diffraction-limited image of mMaple3-HIM-3 before activation. Right: trajectory of a single photoactivated mMaple-3-HIM-3 molecule associated with the axis. Diffraction limited data are from a single epifluorescence image. (B) Selected 100 ms frames of raw data from the molecular trajectory shown in (A). Frame borders are colored according to the time colormap in (A). One plane of biplane data is shown. (C) Left: diffraction-limited image of GFP-HIM-3 reference channel. Right: trajectory of a single photoactivated PAJF549 molecule linked to HTP-3-HaloTag associated with the axis. (D) Histogram of total photon counts and corresponding exponential fits for trajectories of mMaple3-HIM-3 and HTP-3-HaloTag (PAJF549); means indicated at top. (E) Histogram of total lengths in seconds and corresponding exponential fits for trajectories of mMaple3-HIM-3 and HTP-3-HaloTag (PAJF549); means indicated at top. All imaging was performed with 100 ms integration time.

$$\text{MSD}(\tau) = 4D\tau - \frac{4D\Delta t}{3} + 2\sigma_x^2 + 2\sigma_y^2 \tag{1}$$

with frame integration time $\Delta\tau$, lag time $\tau$, diffusion coefficient $D$, and total localization error $(2\sigma_x^2 + 2\sigma_y^2)$ as free parameters determined by using nonlinear least-squares estimation. We used tracks with duration of at least five frames for this analysis and performed linear fits to the first four lags of the MSD plot to avoid bias due to higher standard deviations at longer lags.[37] In addition to estimates of $D$ described in the text, these fits also yielded estimates of the effective localization precision $\sigma_{xy}$ of 126 ± 26 nm (mobile molecules, error is standard deviation of bootstrapped tracks) and 15.5 ± 0.5 nm (bound molecules), which presumably differ due to different degrees of motion blur in these two populations. While mMaple3-HIM-3 tracks were difficult to analyze in this way because of their relatively high rate of bleaching, applying similar analysis to tracks with MJDs < 100 nm and duration of five or more frames yielded an estimate of $\sigma_{xy}$ of 27 ± 11 nm. We corroborated this estimate by measuring the empirical localization precision, analyzing the standard deviation of molecule positions in a relatively stationary subset of the trajectory shown in Figure 2A. In this way, we estimated $\sigma_{xy}$ to be 24.6 nm (Figure S3).

**Registration of Diffraction-Limited and Single-Molecule Imaging Channels.** Fluorescent beads (100 nm TetraSpeck, Invitrogen) were imaged in both the green (reference) and orange (single-molecule) channels. The centers of beads in the reference channel image were mapped to localizations of those beads in the single-molecule channel to generate an affine transformation, which incorporates rotation, scaling, shear, and translation (Figure S4A). The accuracy of this map can be defined by the fiducial registration error (average Euclidean distance between the target positions and positions in the transform); for the data presented here, this value was 23 nm.

## 3. RESULTS

We wished to develop an *ex vivo* imaging protocol that would provide optimal optical properties and dye penetrance and at the same time maintain physiological meiotic progression (Figure 1A). Previous imaging of live worms has shown that meiotic chromosomes undergo dynein-driven motion beginning at meiotic entry. Dynein-driven motion invariably ceases upon starvation or when worms are paralyzed with an anesthetic.[38] Because maintaining a nutrient-rich environment similar to that experienced within animals can preserve oocyte motion in extruded gonads (Figure 1B),[32] we hypothesized this might also allow meiotic functions to continue. By adapting the embryonic culture medium used in previous work[32] and monitoring GFP-labeled HIM-3 protein to follow the axis (Figure 1C,D), we found that nuclei exhibited motion within the gonad and that chromosomes dynamically rearranged for up to an hour after dissection (Figure 1E and Movie S1). Meiotic functions depended on the presence of nutrients available in the culture medium, as nuclei in gonads extruded in physiological saline halted chromosome motion within a few minutes (data not
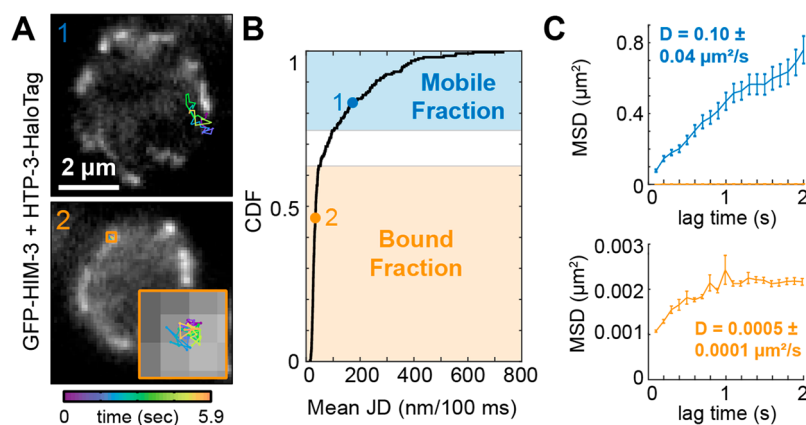
**Figure 3.** Single-molecule tracking of HTP-3 subpopulations with different dynamics. (A) Single-molecule trajectories of HTP-3-HaloTag molecules overlaid onto diffraction-limited reference images of GFP-HIM-3, marking the axis in pachytene nuclei. Top: a trajectory displaying diffusion through the nucleoplasm. Bottom: a static trajectory within a single axis. (B) Cumulative distribution function (CDF) of mean jump displacements (JDs) for HTP-3-HaloTag molecules. Dots on the CDF curve mark the mean jump displacements of the two tracks shown in part A. (C) Mean-squared displacements as a function of lag time for the mobile and bound trajectory populations marked in panel B. Top: mobile fraction ($N = 39$ trajectories). The bound fraction is also plotted for reference, virtually overlapping with the $x$-axis at this scale. Bottom: the bound fraction ($N = 163$ trajectories), with MSD scaled by a factor of 1000. Error bars of each MSD value represent standard error estimated from bootstrapping tracks. Precision of $D$ estimate is the standard deviation when bootstrapping tracks.

shown). This suggests that overall gonad physiology, and thus meiotic function, was preserved under these conditions.

In addition to lowering autofluorescence and optical aberrations, imaging in live extruded gonads exposes the tissue of the gonad to the surrounding buffer. This is attractive for bioorthogonal labeling approaches such as the HaloTag system, in which a genetically encoded enzyme (the HaloTag enzyme) covalently binds the chloroalkyl moiety (HaloTag ligand, HTL) of an added dye.[29] We tested whether we could introduce dyes into the gonad without extending the time required for sample preparation using the dye JF549-HTL[39] to label endogenously expressed HTP-3-HaloTag (Figure 1F). Fully replacing native HTP-3 with the HTP-3-HaloTag partially perturbed meiotic function but did not disrupt the localization of HTP-3 (Methods section, Figure S1). While the addition of dye to the dissection buffer led to background fluorescence when the HaloTag enzyme was not present, expression of endogenous HTP-3-HaloTag fusion protein effectively quenched this excess dye without requiring a washout step or other modifications to our protocol. Notably, while similar bioorthogonal imaging approaches have been successfully used for super-resolution imaging in whole worms, these have required the use of >1000-fold higher dye concentrations and washout steps lasting several hours.[40] This robust and versatile labeling approach expands the toolkit for single-molecule imaging, joining fluorescent tags previously used in worms such as the green-to-red UV-photoconvertible protein mMaple3.[4,23,41]

We characterized the suitability of photoconvertible mMaple3 and the UV-photoactivatable (dark-to-bright) PAJF549 dye[24] for single-molecule imaging in live gonads. We first tested the blinking properties and photostability of mMaple3 fused to HIM-3. By correlating trajectories of photoconverted single molecules with diffraction-limited images of bulk unconverted mMaple3, we confirmed that detected single molecules appeared primarily within the axis (Figure 2A). Examining individual trajectories that appeared within the axis, we detected mMaple3-HIM-3 for up to several seconds (Figure 2A) with a localization precision $\sigma_{xy}$ of ~25 nm (Methods section, Figure S3). These trajectories exhibited digital photoactivation and

photobleaching events as well as occasional brief (≤400 ms) blinking events (Figure 2B and Figure S2A,B). Consistent with previous work using confocal microscopy,[38] the visible laser light we used for single-molecule imaging did not appear to impair meiotic activity, as nuclei and chromosomes continued to exhibit motion during multiminute acquisitions (Methods section, Figure 2C, and Movie S2). Despite this motion, sampling chromosome motion at 30 s intervals was sufficient to contextualize track positions, consistent with previously described root-mean-squared displacements of ≤1.0 $\mu$m/min for chromosomes during the pachytene stage of meiosis (Figure S4B).[28]

We characterized the photophysics of the PAJF549-HTL dye bound to HTP-3-HaloTag using GFP-HIM-3 as a diffraction-limited reference channel (Figure 2C). Crucially, PAJF549 afforded dramatically longer tracks with a greater total number of photons (a mean of 2 s with 100 ms integration time and 8400 photons) compared with mMaple3 (0.7 s and 1200 photons) (Figure 2D,E and Figure S2C). Additionally, PAJF549 could be consistently localized for a larger fraction of each track: for mMaple3, 43% frames of each track fell below the background threshold for localization due to intensity fluctuations (blinking), while for PAJF549, only 22% of frames per track were not localized (Figure S2D). These results are consistent with the greater photostability of photoactivatable dyes relative to fluorescent proteins *in vitro* and in other biological systems.[39,41,42]

The longer single-molecule trajectories that we obtained for PAJF549-labeled HTP-3-HaloTag molecules allowed us to discriminate between several subpopulations of molecules. Overlaying HTP-3-HaloTag trajectories with the GFP-HIM-3 reference channel (Figure 3A) suggested two such populations: a large fraction of static molecules that colocalized with the axes and freely diffusing molecules that did not exhibit a correlation with GFP-HIM-3. To quantify these populations, we calculated the mean jump displacements of each molecule trajectory and analyzed the resulting distribution (Figure 3B). This distribution exhibited an inflection point at a mean jump displacement of ~75 nm. We interpret this as a bound fraction of HTP-3

molecules integrated into the axis (two-thirds of all detected molecules) and a mobile fraction of free molecules (one-third). Because no single cutoff perfectly separated this bimodal distribution, we defined windows for tracks with mean jump displacements of <50 nm and of >100 nm as bound and mobile, respectively. By separately applying mean-squared displacement (MSD) analysis to each subpopulation (Figure 3C), we found that bound molecules exhibited only small amounts of confined motion ($D = 5 \times 10^{-4} \pm 1 \times 10^{-4}$ $\mu m^2/s$ at short times and flattening MSD curves at longer lag times). We estimated a value for the PAJF549 localization precision of $\sigma_{xy} = 15.5 \pm 0.7$ nm from the MSD curve (Methods section). The mobile fraction exhibited Brownian diffusion with diffusion coefficient $D = 0.10 \pm 0.04$ $\mu m^2/s$, with a linear MSD curve even at longer intervals (Figure 3C). These measurements are in the range of diffusion coefficients measured by single-molecule tracking of transcription factors and slower (as expected) than those measured for fluorescent proteins not fused to nuclear proteins.[14,43] These results were only weakly sensitive to the choice of mean jump displacement cutoff used to categorize subpopulations, with values of $D$ increasing 4% for the bound population when the lower threshold was raised to 75 nm and decreasing 21% for the mobile population when the upper threshold was lowered to 75 nm.

Our observation of Brownian diffusion for mobile HTP-3-HaloTag molecules suggests motion was largely unobstructed, at least on the $\leq 1$ $\mu m$ scale (Figure 3C). On larger scales, however, diffusion is likely to be affected by the heterogeneity of the nucleoplasm, which includes, among many other characterized compartments, chromosomes, heterochromatin, and the nucleolus. The latter is perhaps best characterized for its ability to selectively recruit client macromolecules while excluding euchromatin and other macromolecules.[44]

To investigate whether HTP-3 molecules were able to freely explore the entire nucleus, we first examined bulk localization in premeiotic nuclei, where HTP-3 is expressed but has not yet associated with chromatin to form the meiotic axis. Confocal slices of nuclei immunolabeled for HTP-3 alongside DAPI and the nucleolar marker DAO-5[45] allowed us to demarcate the localization pattern of HTP-3 relative to the chromosomes and to the nucleolus, which in the worm germline forms a sphere filling the middle of the nucleus (Figure 1C and Figure 4A, top). Averaging protein distributions from multiple nuclei within a shared coordinate system did not show a significant difference of HTP-3 density in the nucleolus (Figure 4A, top). However, as has been shown for transcription factors in embryonic stem cells, fixation can bias the observed distribution of chromatin-associated proteins away from DNA.[12] Repeating this experiment in live gonads using genetically encoded mChy-H2B as a marker for chromatin, we found that GFP-HTP-3 was depleted from the center of the nucleus (Figure 4A, bottom), indicating that prior to axis assembly axis proteins are partitioned away from the nucleolus and into chromatin-rich regions.

Our single-molecule approach allowed us study a more physiologically relevant scenario: the diffusion of unbound molecules at a time when a protein of interest exhibits a well-defined localization pattern on chromatin. We returned to pachytene nuclei and used our single-molecule data to examine the specific case of HTP-3 molecules that were not associated with chromatin (the mobile fraction as defined in Figure 3). We found that these tracks were preferentially partitioned away from the nucleolus, with a distribution similar to that in the premeiotic live-cell case (Figure 4B). This suggests that
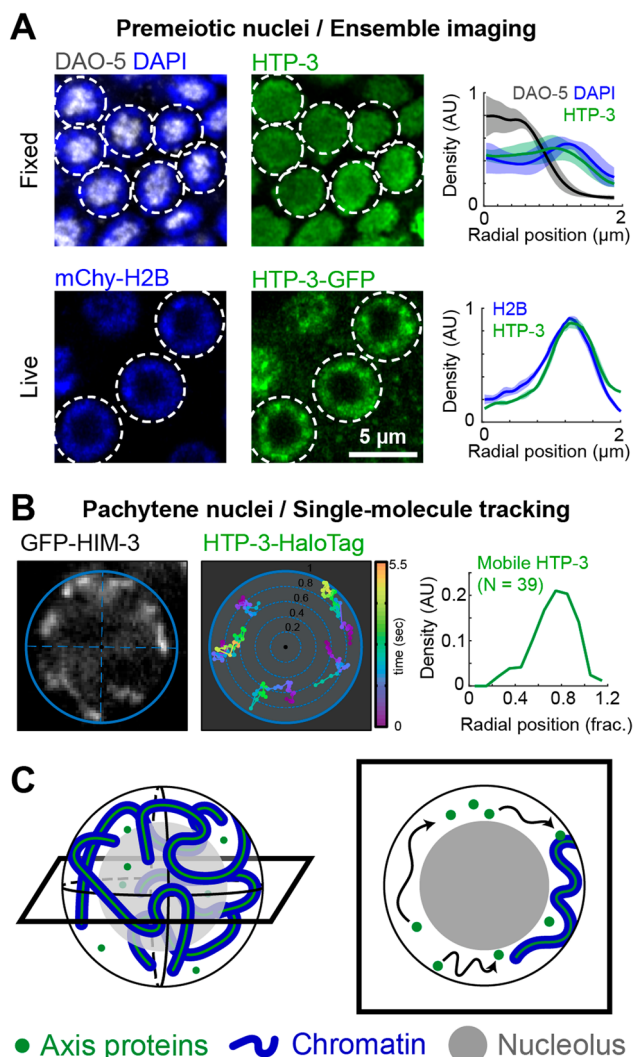


**Figure 4.** The nucleolus excludes HTP-3 molecules. (A) Confocal imaging of free axis proteins (HTP-3) relative to DNA (DAPI, mChy-H2B) and the nucleolus (DAO-5) in premeiotic nuclei. Top: immunolabeling of fixed gonads. Bottom: imaging in live extruded gonads. White circles: nuclei used to generate profiles of radial density, shown on the right. Each line, mean of density profiles in indicated nuclei; shaded areas, standard deviation. (B) Distribution of single-molecule tracks of HTP-3 in meiotic (pachytene) nuclei. Left: example ellipse drawn onto diffraction-limited GFP-HIM-3 reference image to define nuclear coordinates. Middle: five tracks registered within the shared polar coordinate system. Right: distribution of mobile HTP-3 molecule localizations from 39 tracks. (C) Schematic of axis protein dynamics within pachytene nuclei. Left: three-dimensional nuclear geometry, with cross section shown on the right. Mobile axis proteins are excluded from the nucleolus and must diffuse in the nuclear periphery (black arrows) to find binding sites on chromosomes.

chromatin-associated proteins are selectively excluded from the nucleolus, requiring their diffusion to circumvent the center of the nucleus and specifically traverse chromatin-rich regions. Nucleolar occlusion could impact search kinetics: in the case of meiotic *C. elegans* nuclei, search would occur in a shell at the periphery of the nucleus rather than throughout the full nuclear volume (Figure 4C).

## 5. DISCUSSION

In this work, we established an approach to image extruded *C. elegans* gonads. This system allowed us to probe nuclei actively undergoing meiosis using single-molecule imaging. In addition to avoiding autofluorescence common when imaging whole animals, our method allowed us to use a variety of newly developed labels and synthetic dyes. We quantitated the photophysics of both mMaple3 and HaloTag-bound PAJF549 when fused to proteins of the meiotic axis and found that while both labels were suitable for single-molecule tracking, the greater photostability of PAJF549 supported categorization of heterogeneous molecular diffusivities. Sifting tracks by diffusivity allowed us to analyze the distribution of mobile, free molecules of the axis protein HTP-3 and to show that their diffusion trajectories sidestep the nucleolus.

Successful execution of the meiotic program requires dramatic remodeling of chromosomes and tightly regulated production of chromosomal crossovers[28], [38], and [46–48]. While these dynamic processes are integral to meiosis, super-resolution imaging of chromosome structure and DNA repair intermediates has been mostly limited to fixed samples,[4,49] and there have been only a few studies investigating molecular turnover within meiotic structures.[23,26,50,51] In this work, we apply single-molecule tracking to study the dynamic behavior of chromatin-associated molecules. This revealed the underlying flow of an otherwise difficult to detect subpopulation of freely diffusing molecules. The *ex vivo* gonad preparation we have optimized here allowed us to use newly developed dyes and an optically advantageous sample while maintaining physiological meiotic function. Future work, taking advantage of the transparency and size of *C. elegans*, recent progress in immobilization procedures,[38,52] and the development of novel synthetic dyes and fluorescent proteins[53] should enable to extend our approach to live, intact animals.

Single-molecule tracking has shown that chromatin-associated proteins such as transcription factors exhibit multiple search types (e.g., one-dimensional diffusion along chromatin, transient interactions, and three-dimensional diffusion) and that these are affected by the local nuclear environment.[14,43,54] Our approach promises to expand the scope of these studies to complex biological processes that occur in whole tissues and animals. Some of the meiosis-specific processes that are likely to benefit from the rich information generated by single-molecule tracking include chromatin remodeling during axis assembly,[3] the liquid-like organization of the synaptonemal complex,[23,50,51] and the recruitment of repair proteins to prospective crossover sites.[55]

Biomolecular phase separation has recently emerged as a provocative new framework to understand cellular organization and signaling. Phase separation in the nucleus appears to play a role in diverse aspects of biology including development, neuronal function, and immunology.[56–58] Indeed, fundamental components of the nucleus can be viewed as phase-separated entities, and recent work has shown that a diffusion boundary exists between euchromatin and heterochromatin[59] and that the nucleolus is composed of multiple phase-separated subdomains.[44] However, with few exceptions, these studies have focused on the composition of phase-separated membraneless organelles and the consequences of sequestration within them. Here we have shown that membraneless organelles also influence their surroundings: by being unable to enter the nucleolus, meiotic axis-associated proteins must traverse the nuclear periphery, effectively sequestering and enriching them where chromosomes are located. The application of single-molecule tracking promises to reveal further functions of phase-separated entities within cells.

## ASSOCIATED CONTENT

**Supporting Information**

The Supporting Information is available free of charge at https://pubs.acs.org/doi/10.1021/acs.jpcb.1c03040.

Figures S1−S4 (PDF)
Movie S1 (AVI)
Movie S2 (AVI)

## AUTHOR INFORMATION

**Corresponding Authors**

**Lexy von Diezmann** − *Center for Cell and Genome Sciences and School of Biological Sciences, University of Utah, Salt Lake City, Utah 84112, United States;* orcid.org/0000-0001-8364-0027; Email: lexy.diezmann@utah.edu

**Ofer Rog** − *Center for Cell and Genome Sciences and School of Biological Sciences, University of Utah, Salt Lake City, Utah 84112, United States;* Email: ofer.rog@utah.edu

Complete contact information is available at:
https://pubs.acs.org/10.1021/acs.jpcb.1c03040

**Notes**
The authors declare no competing financial interest.

## REFERENCES

(1) Zickler, D.; Kleckner, N. Meiotic Chromosomes: Integrating Structure and Function. *Annu. Rev. Genet.* **1999**, 33 (1), 603−754.

(2) Page, S. L.; Hawley, R. S. The Genetics and Molecular Biology of the Synaptonemal Complex. *Annu. Rev. Cell Dev. Biol.* **2004**, 20, 525−558.

(3) Kim, Y.; Rosenberg, S. C.; Kugel, C. L.; Kostow, N.; Rog, O.; Davydov, V.; Su, T. Y.; Dernburg, A. F.; Corbett, K. D. The Chromosome Axis Controls Meiotic Events through a Hierarchical Assembly of HORMA Domain Proteins. *Dev. Cell* **2014**, 31 (4), 487−502.

(4) Köhler, S.; Wojcik, M.; Xu, K.; Dernburg, A. F. Superresolution Microscopy Reveals the Three-Dimensional Organization of Meiotic Chromosome Axes in Intact *Caenorhabditis Elegans* Tissue. *Proc. Natl. Acad. Sci. U. S. A.* **2017**, 114 (24), E4734−E4743.

(5) Syrjänen, J. L.; Pellegrini, L.; Davies, O. R. A Molecular Model for the Role of SYCP3 in Meiotic Chromosome Organisation. *eLife* **2014**, 3, 1−18.

(6) Rog, O.; Dernburg, A. F. Chromosome Pairing and Synapsis during Caenorhabditis Elegans Meiosis. *Curr. Opin. Cell Biol.* **2013**, *25* (3), 349−356.

(7) Phillips, C. M.; McDonald, K. L.; Dernburg, A. F. Cytological Analysis of Meiosis in Caenorhabditis Elegans. *Methods Mol. Biol.* **2009**, *558*, 171−195.

(8) Woglar, A.; Yamaya, K.; Roelens, B.; Boettiger, A.; Köhler, S.; Villeneuve, A. M. Quantitative Cytogenetics Reveals Molecular Stoichiometry and Longitudinal Organization of Meiotic Chromosome Axes and Loops. *PLoS Biol.* **2020**, *18* (8), No. e3000817.

(9) Chong, S.; Dugast-Darzacq, C.; Liu, Z.; Dong, P.; Dailey, G. M.; Cattoglio, C.; Heckert, A.; Banala, S.; Lavis, L.; Darzacq, X.; Tjian, R. Imaging Dynamic and Selective Low-Complexity Domain Interactions That Control Gene Transcription. *Science (Washington, DC, U. S.)* **2018**, *361* (6400), eaar2555.

(10) Cho, W.; Spille, J.; Hecht, M.; Lee, C.; Li, C.; Grube, V.; Cisse, I. I. Mediator and RNA Polymerase II Clusters Associate in Transcriptiondependent Condensates. *Science (Washington, DC, U. S.)* **2018**, *361*, 412−415.

(11) Jones, D. L.; Leroy, P.; Unoson, C.; Fange, D.; Ćurić, V.; Lawson, M. J.; Elf, J. Kinetics of DCas9 Target Search in Escherichia Coli. *Science (Washington, DC, U. S.)* **2017**, *357* (6358), 1420−1424.

(12) Teves, S. S.; An, L.; Hansen, A. S.; Xie, L.; Darzacq, X.; Tjian, R. A Dynamic Mode of Mitotic Bookmarking by Transcription Factors. *eLife* **2016**, *5*, 1−24.

(13) Sabari, B. R.; Dall'Agnese, A.; Boija, A.; Klein, I. A.; Coffey, E. L.; Shrinivas, K.; Abraham, B. J.; Hannett, N. M.; Zamudio, A. V.; Manteiga, J. C.; Li, C. H.; Guo, Y. E.; Day, D. S.; Schuijers, J.; Vasile, E.; Malik, S.; Hnisz, D.; Lee, T. I.; Cisse, I. I.; Roeder, R. G.; Sharp, P. A.; Chakraborty, A. K.; Young, R. A. Coactivator Condensation at Super-Enhancers Links Phase Separation and Gene Control. *Science (Washington, DC, U. S.)* **2018**, *361* (6400), eaar3958.

(14) Izeddin, I.; Récamier, V.; Bosanac, L.; Cissé, I. I.; Boudarene, L.; Dugast-Darzacq, C.; Proux, F.; Bénichou, O.; Voituriez, R.; Bensaude, O.; Dahan, M.; Darzacq, X. Single-Molecule Tracking in Live Cells Reveals Distinct Target-Search Strategies of Transcription Factors in the Nucleus. *eLife* **2014**, *3*, 1−27.

(15) Cuvier, O.; Fierz, B. Dynamic Chromatin Technologies: From Individual Molecules to Epigenomic Regulation in Cells. *Nat. Rev. Genet.* **2017**, *18* (8), 457−472.

(16) von Diezmann, A.; Shechtman, Y.; Moerner, W. E. Three-Dimensional Localization of Single Molecules for Super- Resolution Imaging and Single-Particle Tracking. *Chem. Rev.* **2017**, *117*, 7244−7275.

(17) Varela, J. A.; Dupuis, J. P.; Etchepare, L.; Espana, A.; Cognet, L.; Groc, L. Targeting Neurotransmitter Receptors with Nanoparticles in Vivo Allows Single-Molecule Tracking in Acute Brain Slices. *Nat. Commun.* **2016**, *7*, 1−10.

(18) Mashanov, G. I.; Nenasheva, T. A.; Mashanova, T.; Maclachlan, C.; Birdsall, N. J. M.; Molloy, J. E. A Method for Imaging Single Molecules at the Plasma Membrane of Live Cells within Tissue Slices. *J. Gen. Physiol.* **2021**, DOI: 10.1085/jgp.202012657.

(19) Schaaf, M. J. M.; Koopmans, W. J. A.; Meckel, T.; Van Noort, J.; Snaar-Jagalska, B. E.; Schmidt, T. S.; Spaink, H. P. Single-Molecule Microscopy Reveals Membrane Microdomain Organization of Cells in a Living Vertebrate. *Biophys. J.* **2009**, *97* (4), 1206−1214.

(20) Mir, M.; Reimer, A.; Haines, J. E.; Li, X. Y.; Stadler, M.; Garcia, H.; Eisen, M. B.; Darzacq, X. Dense Bicoid Hubs Accentuate Binding along the Morphogen Gradient. *Genes Dev.* **2017**, *31* (17), 1784−1794.

(21) Robin, F. B.; McFadden, W. M.; Yao, B.; Munro, E. M. Single-Molecule Analysis of Cell Surface Dynamics in Caenorhabditis Elegans Embryos. *Nat. Methods* **2014**, *11* (6), 677−682.

(22) Wu, Y.; Han, B.; Gauvin, T. J.; Smith, J.; Singh, A.; Griffin, E. E. Single-Molecule Dynamics of the P Granule Scaffold MEG-3 in the Caenorhabditis Elegans Zygote. *Mol. Biol. Cell* **2019**, *30* (3), 333−345.

(23) Rog, O.; Köhler, S.; Dernburg, A. F. The Synaptonemal Complex Has Liquid Crystalline Properties and Spatially Regulates Meiotic Recombination Factors. *eLife* **2017**, *6*, No. e21455.

(24) Grimm, J. B.; English, B. P.; Choi, H.; Muthusamy, A. K.; Mehl, B. P.; Dong, P.; Brown, T. A.; Lippincott-Schwartz, J.; Liu, Z.; Lionnet, T.; Lavis, L. D. Bright Photoactivatable Fluorophores for Single-Molecule Imaging. *Nat. Methods* **2016**, *13* (12), 985−988.

(25) Brenner, S. The Genetics of *Caenorhabditis Elegans*. *Genetics* **1974**, *77*, 71−94.

(26) Stauffer, W. T.; Zhang, L.; Dernburg, A. Diffusion through a Liquid Crystalline Compartment Regulates Meiotic Recombination. *Proc. SPIE* **2019**, *10888*.

(27) Kim, Y.; Kostow, N.; Dernburg, A. F. The Chromosome Axis Mediates Feedback Control of CHK-2 to Ensure Crossover Formation in *C. Elegans*. *Dev. Cell* **2015**, *35* (2), 247−261.

(28) Wynne, D. J.; Rog, O.; Carlton, P. M.; Dernburg, A. F. Dynein-Dependent Processive Chromosome Motions Promote Homologous Pairing in *C. Elegans* Meiosis. *J. Cell Biol.* **2012**, *196* (1), 47−64.

(29) Los, G. V.; Encell, L. P.; Mcdougall, M. G.; Hartzell, D. D.; Karassina, N.; Simpson, D.; Mendez, J.; Zimmerman, K.; Otto, P.; Vidugiris, G.; Zhu, J.; Darzins, A.; Klaubert, D. H.; Bulleit, R. F.; Wood, K. V.; et al. HaloTag: A Novel Protein Labeling Technology for Cell Imaging and Protein Analysis. *ACS Chem. Biol.* **2008**, *3* (6), 373−382.

(30) Aljohani, M. D.; El Mouridi, S.; Priyadarshini, M.; Vargas-Velazquez, A. M.; Frøkjær-Jensen, C. Engineering Rules That Minimize Germline Silencing of Transgenes in Simple Extrachromosomal Arrays in *C. Elegans*. *Nat. Commun.* **2020**, *11* (1), 1−14.

(31) MacQueen, A. J.; Phillips, C. M.; Bhalla, N.; Weiser, P.; Villeneuve, A. M.; Dernburg, A. F. Chromosome Sites Play Dual Roles to Establish Homologous Synapsis during Meiosis in *C. Elegans*. *Cell* **2005**, *123* (6), 1037−1050.

(32) Wolke, U.; Jezuit, E. A.; Priess, J. R. Actin-Dependent Cytoplasmic Streaming in *C. Elegans* Oogenesis. *Development* **2007**, *134* (12), 2227−2236.

(33) Avery, L.; Raizen, D.; Lockery, S. Electrophysiological Methods. In *Methods in Cell Biology*; Elsevier: 1995; Vol. 48, pp 251−269.

(34) Juette, M. F.; Gould, T. J.; Lessard, M. D.; Mlodzianoski, M. J.; Nagpure, B. S.; Bennett, B. T.; Hess, S. T.; Bewersdorf, J. Three-Dimensional Sub-100 Nm Resolution Fluorescence Microscopy of Thick Samples. *Nat. Methods* **2008**, *5* (6), 527−529.

(35) Huang, F.; Hartwich, T. M. P.; Rivera-Molina, F. E.; Lin, Y.; Duim, W. C.; Long, J. J.; Uchil, P. D.; Myers, J. R.; Baird, M. A.; Mothes, W.; Davidson, M. W.; Toomre, D.; Bewersdorf, J. Video-Rate Nanoscopy Using SCMOS Camera-Specific Single-Molecule Localization Algorithms. *Nat. Methods* **2013**, *10* (7), 653−658.

(36) Lasker, K.; von Diezmann, L.; Zhou, X.; Ahrens, D. G.; Mann, T. H.; Moerner, W. E.; Shapiro, L. Selective Sequestration of Signalling Proteins in a Membraneless Organelle Reinforces the Spatial Regulation of Asymmetry in *Caulobacter Crescentus*. *Nat. Microbiol.* **2020**, *5* (3), 418−429.

(37) Michalet, X.; Berglund, A. J. Optimal Diffusion Coefficient Estimation in Single-Particle Tracking. *Phys. Rev. E - Stat. Nonlinear, Soft Matter Phys.* **2012**, *85* (6), 1−14.

(38) Rog, O.; Dernburg, A. F. Direct Visualization Reveals Kinetics of Meiotic Chromosome Synapsis. *Cell Rep.* **2015**, *10* (10), 1639−1645.

(39) Grimm, J. B; English, B. P; Choi, H.; Muthusamy, A. K; Mehl, B. P; Dong, P.; Brown, T. A; Lippincott-Schwartz, J.; Liu, Z.; Lionnet, T.; Lavis, L. D Bright Photoactivatable Fluorophores for Single-Molecule Imaging. *Nat. Methods* **2016**, *13* (12), 985−988.

(40) Li, P.; Merrill, S. A.; Jorgensen, E. M.; Shen, K. Two Clathrin Adaptor Protein Complexes Instruct Axon-Dendrite Polarity. *Neuron* **2016**, *90* (3), 564−580.

(41) Wang, S.; Moffitt, J. R.; Dempsey, G. T.; Xie, X. S.; Zhuang, X. Characterization and Development of Photoactivatable Fluorescent Proteins for Single-Molecule-Based Superresolution Imaging. *Proc. Natl. Acad. Sci. U. S. A.* **2014**, *111* (23), 8452−8457.

(42) Lee, H. L. D.; Lord, S. J.; Iwanaga, S.; Zhan, K.; Xie, H.; Williams, J. C.; Wang, H.; Bowman, G. R.; Goley, E. D.; Shapiro, L.; Twieg, R. J.; Rao, J.; Moerner, W. E. Superresolution Imaging of Targeted Proteins in Fixed and Living Cells Using Photoactivatable Organic Fluorophores. *J. Am. Chem. Soc.* **2010**, *132* (43), 15099−15101.

(43) Li, L.; Liu, H.; Dong, P.; Li, D.; Legant, W. R.; Grimm, J. B.; Lavis, L. D.; Betzig, E.; Tjian, R.; Liu, Z. Real-Time Imaging of Huntingtin Aggregates Diverting Target Search and Gene Transcription. *eLife* **2016**, *5*, 1−29.

(44) Lafontaine, D. L. J.; Riback, J. A.; Bascetin, R.; Brangwynne, C. P. The Nucleolus as a Multiphase Liquid Condensate. *Nat. Rev. Mol. Cell Biol.* **2021**, *22* (March), 165−182.

(45) Lee, C. C.; Tsai, Y. T.; Kao, C. W.; Lee, L. W.; Lai, H. J.; Ma, T. H.; Chang, Y. S.; Yeh, N. H.; Lo, S. J. Mutation of a Nopp140 Gene Dao-5 Alters RDNA Transcription and Increases Germ Cell Apoptosis in *C. Elegans*. *Cell Death Dis.* **2014**, *5* (4), e1158.

(46) Marshall, W. F; Fung, J. C Modeling Meiotic Chromosome Pairing: Nuclear Envelope Attachment, Telomere-Led Active Random Motion, and Anomalous Diffusion. *Phys. Biol.* **2016**, *13* (2), 026003.

(47) Koszul, R.; Kim, K. P.; Prentiss, M.; Kleckner, N.; Kameoka, S. Meiotic Chromosomes Move by Linkage to Dynamic Actin Cables with Transduction of Force through the Nuclear Envelope. *Cell* **2008**, *133* (7), 1188−1201.

(48) Conrad, M. N.; Lee, C. Y.; Chao, G.; Shinohara, M.; Kosaka, H.; Shinohara, A.; Conchello, J. A.; Dresser, M. E. Rapid Telomere Movement in Meiotic Prophase Is Promoted By NDJ1, MPS3, and CSM4 and Is Modulated by Recombination. *Cell* **2008**, *133* (7), 1175−1187.

(49) Woglar, A.; Villeneuve, A. M. Dynamic Architecture of DNA Repair Complexes and the Synaptonemal Complex at Sites of Meiotic Recombination. *Cell* **2018**, *173* (7), 1678−1691.

(50) Pattabiraman, D.; Roelens, B.; Woglar, A.; Villeneuve, A. M. Meiotic Recombination Modulates the Structure and Dynamics of the Synaptonemal Complex during *C. Elegans* Meiosis. *PLoS Genet.* **2017**, *13* (3), No. e1006670.

(51) Nadarajan, S.; Lambert, T. J.; Altendorfer, E.; Gao, J.; Blower, M. D.; Waters, J. C.; Colaiácovo, M. P. Polo-like Kinase-Dependent Phosphorylation of the Synaptonemal Complex Protein SYP-4 Regulates Double-Strand Break Formation through a Negative Feedback Loop. *eLife* **2017**, *6*, 1−25.

(52) Burnett, K.; Edsinger, E.; Albrecht, D. R. Rapid and Gentle Hydrogel Encapsulation of Living Organisms Enables Long-Term Microscopy over Multiple Hours. *Commun. Biol.* **2018**, *1* (1), 73.

(53) Li, H.; Vaughan, J. C. Switchable Fluorophores for Single-Molecule Localization Microscopy. *Chem. Rev.* **2018**, *118* (18), 9412−9454.

(54) Brown, M. W.; Kim, Y.; Williams, G. M.; Huck, J. D.; Surtees, J. A.; Finkelstein, I. J. Dynamic DNA Binding Licenses a Repair Factor to Bypass Roadblocks in Search of DNA Lesions. *Nat. Commun.* **2016**, *7*, 1−12.

(55) Zhang, L.; Köhler, S.; Rillo-Bohn, R.; Dernburg, A. F. A Compartmentalized Signaling Network Mediates Crossover Control in Meiosis. *eLife* **2018**, *7*, No. e30789.

(56) Alberti, S. The Wisdom of Crowds: Regulating Cell Function through Condensed States of Living Matter. *J. Cell Sci.* **2017**, DOI: 10.1242/jcs.200295.

(57) Yoo, H.; Triandafillou, C.; Drummond, D. A. Cellular Sensing by Phase Separation: Using the Process, Not Just the Products. *J. Biol. Chem.* **2019**, *294* (18), 7151−7159.

(58) Chen, X.; Wu, X.; Wu, H.; Zhang, M. Phase Separation at the Synapse. *Nat. Neurosci.* **2020**, *23* (3), 301−310.

(59) Strom, A. R.; Emelyanov, A. V.; Mir, M.; Fyodorov, D. V.; Darzacq, X.; Karpen, G. H. Phase Separation Drives Heterochromatin Domain Formation. *Nature* **2017**, *547* (7662), 241−245.